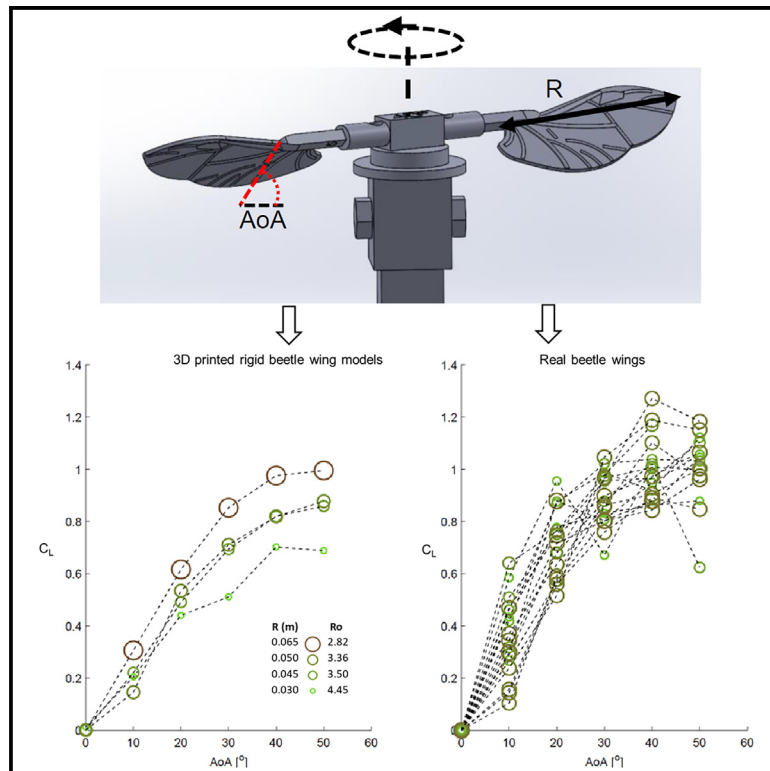# iScience

Insect wing flexibility improves the aerodynamic performance of small revolving wings

Graphical abstract

Authors

Gal Ribak, Ori Stearns,
Kiruthika Sundararajan,
Duvall Dickerson-Evans, Dana Melamed,
Maya Rabinovich, Roi Gurka

Correspondence

gribak@tauex.tau.ac.il (G.R.),
rgurka@coastal.edu (R.G.)

In brief

Biological sciences; Biomimetics;
Biomechanics; Aerodynamics

Highlights

- Aerodynamic performance decreases with diminishing size of rigid propeller blades

- Revolving beetle wings defy the decrease in performance with reduced size

- Wing flexibility scales to maintain performance by improving flow attachment

- Wing flexibility is tuned through adjustment of wing-vein cross-sections

CellPress

Article

Insect wing flexibility improves the aerodynamic performance of small revolving wings

Gal Ribak,[1,2,4,*] Ori Stearns,[1] Kiruthika Sundararajan,[3] Duvall Dickerson-Evans,[3] Dana Melamed,[1] Maya Rabinovich,[1] and Roi Gurka[3,*]

[1]School of Zoology, Faculty of Life Sciences, Tel Aviv University, Tel Aviv 6997801, Israel
[2]Steinhardt Museum of Natural History, Tel Aviv 6997801, Israel
[3]Department of Physics and Engineering Science, Coastal Carolina University, Conway, SC 29526, USA
[4]Lead contact
*Correspondence: gribak@tauex.tau.ac.il (G.R.), rgurka@coastal.edu (R.G.)
https://doi.org/10.1016/j.isci.2025.112035

SUMMARY

Insect wings are flexible, elastically deforming under loads experienced during flapping. The adaptive value of this flexibility was tested using a revolving wing set-up. We show that the wing flexibility of the beetle *Batocera rufomaculata* suppresses the reduction in lift coefficient that is expected to occur with a reduction of wing size compared to rigid propeller blades. Moreover, the scaling of wing flexibility with size is intra-specifically tuned through changes in wing-vein cross-section, resulting in smaller wings achieving proportionally larger chordwise deformations compared to larger wings, when loaded with aerodynamic forces. These elastic deformations control the separation of flow from the wing as a function of angle-of-attack, as evidenced by the turbulence activity in the flow field directly beneath the revolving wings. The study underlines the contribution of flexibility to control the flow over insect wings through passive wing deformations without the need for input or feedback from the nervous system.

INTRODUCTION

Insect wings are thin structures that undergo extensive deformations during flapping due to the inertial and aerodynamic loads acting on them.[1–3] Insect-inspired flapping[4] or flapping-rotary[5,6] miniature aerial vehicles use flexible wings as well. Flexibility enables relatively flat wings to passively twist and achieve positive camber during both the upstroke and the downstroke, contributing to their ability to generate lift throughout the flapping cycle.[7–9] The compliance of insect wings to the loads acting on them leads to an aeroelastic coupling between elastic wing deformation and the surrounding flow.[10–15] Insect wings likely evolved to correspond to the fluid-structure interaction (FSI) associated with this coupling, leading biologists and engineers to dedicate substantial efforts to understanding both the beneficial and the deleterious effects of wing flexibility on flapping flight aerodynamics (see[16–18] and references therein). The results of such studies have sometimes been conflicting, with some showing improved performance of flexible wings[19–24] and others showing a reduced performance relative to rigid wings.[25–27] Many of these studies used CFD simulations or empirical testing on mechanical models (e.g.,[10,12,22,26,28–31]). Less is known about the subtle details of the FSI in real insect wings, whose mechanical properties and anatomy are more complex than the mechanical or computational models used. Insect wing flexibility includes spanwise and chordwise flexural stiffness gradients and

the wings' flexural stiffness scales interspecifically with the 3rd and 2nd power of wing length and chord, respectively, when measured by static bending.[32] A study measuring the dynamic wing deformations of the beetle *Protaetia cuprea* during flight found that these deformations are conserved within a 3-fold increase in beetle body mass. This suggests that, intra-specifically, the chordwise stiffness of the beetle's wings grows with the 4th power of the wing's chord length,[33] indicating that larger wings are proportionally stiffer than expected based on the inter-specific scaling relationship.

Although not sharing the full complexity of vortex shedding and wake capture at stroke reversals,[34,35] revolving wings, i.e., wings that rotate about their root like propeller blades, share some similarity with root flapping in the sense that in both cases the wings experience a spanwise gradient in the streamwise velocity. Under these conditions, a thin wing revolving at a constant angle-of-attack (AoA) can generate a stable leading edge vortex (LEV), contributing to a low-pressure region above the wing that augments lift production.[36–40] The lift can be measured as the vertical force generated by wings revolving in a horizontal plane. The lift-coefficient of the revolving wings for a given AoA can be calculated from the measured vertical force as:

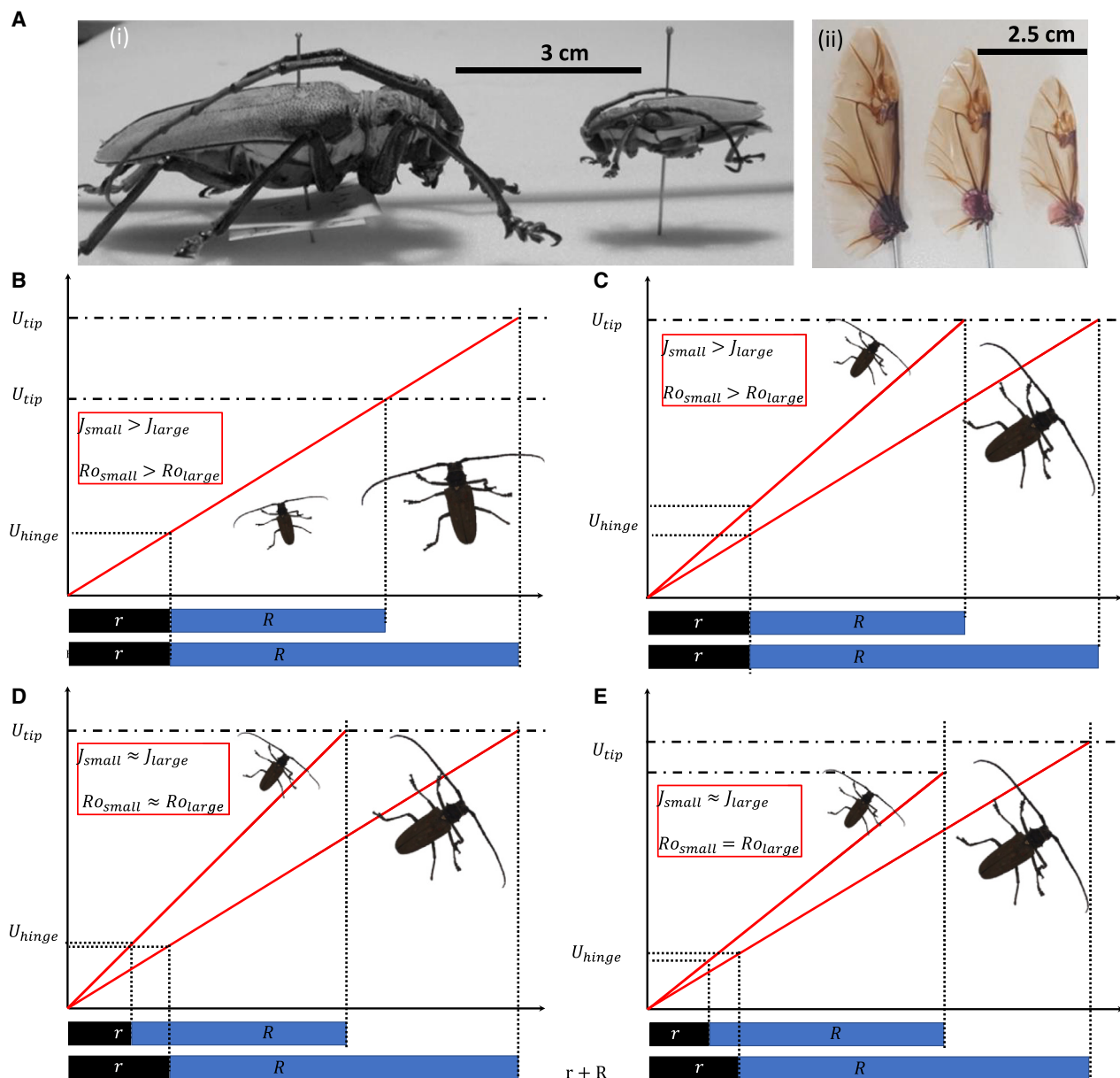$$C_L = \frac{2\overline{L}}{\rho S_2 \Omega^2}$$

Figure 1. Intraspecific variation in insect size affects wing aerodynamics

(A) Two adult males of the beetle *B. rufomaculata* displaying extreme variance in adult body size within this species (i). The variation in body mass is accompanied with variation in wing size ($3 < R < 6$ cm) but not wing shape as exemplified in (ii) showing wings from large, medium, and small conspecifics.

(B–E) Conceptual (qualitative) presentations in which the schematic illustrations explain differences in the spanwise velocity distribution on revolving wings with the same aspect ratio but differing in wing length R (blue horizontal bars) and with an offset (r, black horizontal bar) from the axis of rotation. The vertical axes represent speed relative to air. (B) and (C) depict hypothetical scenarios in which r is the same for the small and large wings, whereas in (D) and (E), the r is scaled according to wing length to retain the same effective aspect ratio $\left(\frac{r+R}{c}\right)$ for the small and large wings. In all cases of $r > 0$, the offset increases the effective aspect ratio, which is proportional to the Ro number of the revolving wings and results in the anatomical wing hinge having a non-zero tangential velocity (U_{hinge}). $U_{\text{hinge}} > 0$ is a condition that occurs also in forward flight and can be described by the advance ratio, using the ratio of the wing speed at the hinge and tip $\left(J = \frac{\text{flight speed}}{\text{wing flapping speed}} = \frac{U_{\text{hinge}}}{U_{\text{tip}}}\right)$. (B) Small and large wings with the same r, revolving at the same angular velocity (Ω), share a similarity with small and large beetles flying at the same flight speed and flapping frequency. In this case, both J and Ro are higher in the smaller beetle. (C) Increasing Ω of the smaller wings to reach the same U_{tip} as that of the large wing. The equivalent is the smaller beetle flapping its wings at a higher frequency and flying faster compared to a larger beetle. The Ro and J will be larger for the smaller wing and beetle. (D) A smaller r and larger Ω for the smaller wing can provide a similar Ro and J as the larger one, either by having the same U_{tip} and U_{hinge} or (E) by having both parameters smaller compared to the large wing. For cases (C–E), i.e., all cases in which the smaller insects have higher flapping frequency, the spanwise velocity gradient over the wing is steeper in the smaller wing.
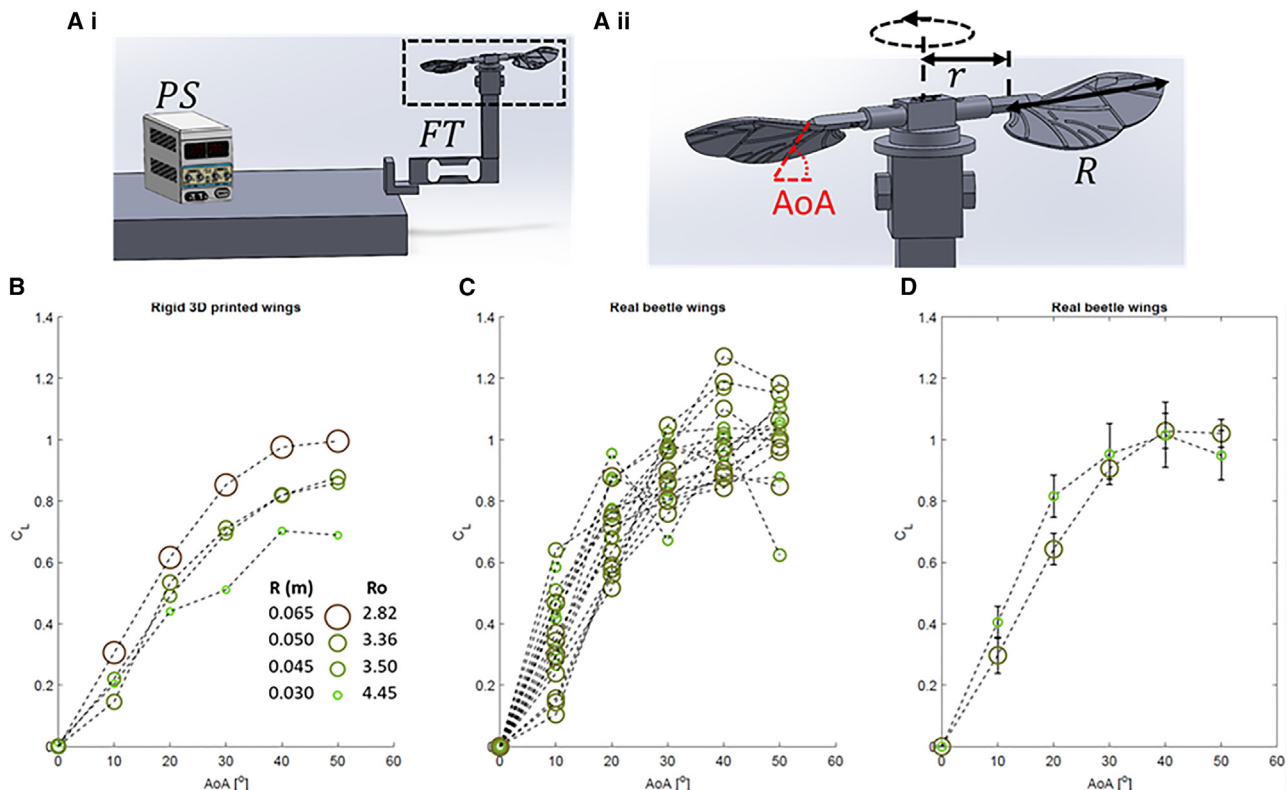
Figure 2. The lift coefficient (C_L) of revolving wings as a function of angle of attack (AoA) and wing size (R)

(A) The revolving wing set-up comprises an electrical power source (PS) powering a DC motor that rotates a pair of beetle wings in a horizontal plane. The motor and wings are mounted on a force transducer (FT) that provides a continuous recording of the vertical force at 100 samples per second. The dashed rectangular area in Ai is enlarged in Aii to depict the definition of wing length (R), wing offset (r), and wing angle of attack (AoA).

(B–D) C_L as a function of AoA in wings differing in size (R [m], denoted by circle colors and size). (B) In rigid, 3D-printed wings, smaller wings display a reduction in C_L as expected from their higher Ro number. (C) Real beetle wings ($n = 20$) differing in size ($0.035 < R < 0.057$ m) do not display a similar decrease in C_L in smaller wings. (D) The C_L of "small" (mean $R \pm SE = 0.038 \pm 0.0015$ m) versus "large" ($R = 0.055 \pm 0.0002$ m) real beetle wings. Each circle in (B) and (C) denote a single measurement, whereas circles in (D) are the mean of measurements from six wing pairs, and the error bars are the standard error of means.

where $\overline{L}$ is the measured vertical force, averaged over time, ρ is air density (taken to be 1.2 kg m^{-3}), S_2 is the second moment of area for the wing pair, and Ω is the angular velocity.[36] The non-dimensional C_L, and how it changes as a function of AoA, describe the aerodynamic performance of the wings. The effective aspect ratio, i.e., the radial distance from the axis of revolution to the wing tip divided by the wing's mean chord lengths, is sometimes referred to as the Rossby number (Ro, but see Data S1—Similarity between the Rossby number and advance ratio, for the distinction between Ro and effective aspect ratio). Ro is inversely related to the aerodynamic performance of the revolving wings since smaller Ro numbers are associated with higher stability of the LEV, leading to higher C_L for a given AoA.[37,41–46] In empirical set-ups, the revolving wings are typically mounted at a small offset between the rotation axis and the anatomical wing hinge. This offset increases the Ro number of the revolving wing set-up, resulting in a more proximal separation of the LEV toward the wing-tip vortex and a reduction in lift production.[42,44,47] The hinge offset also leads to non-zero tangential velocity at the anatomical wing root, a condition that shares some similarity with the spanwise velocity distribu-

tion on the wing during forward flight.[48] The non-dimensional advance ratio, J (=flight speed/wing flapping speed), is typically used to describe the effect of flight speed on the kinematics and aerodynamics of flapping or revolving wings.[49,50] The effect of J on the scaling of aerodynamics during forward flight remains a major knowledge gap in insect flight research.

Differences in resource availability during larval growth can lead to large intraspecific variation in the adult body size of insects. Although wing size should increase with adult body size in order to retain flight capabilities, different scaling relationships can affect the flight performance of small and large conspecifics. In addition to scaling the planform geometry of the wing (wing length and area), the aerodynamic performance of the wings may scale differently between small and large wings as a result of differences in the flow conditions. For instance, it is unclear how the stability of the LEV is affected by larger wing size in larger conspecifics. This increase in size is typically associated with a decrease in flapping frequency, resulting in changes in spanwise flow distribution over the wings (Figure 1). Studies focusing on the scaling of aerodynamic performance often assume that the wings are rigid, thus providing insight into the
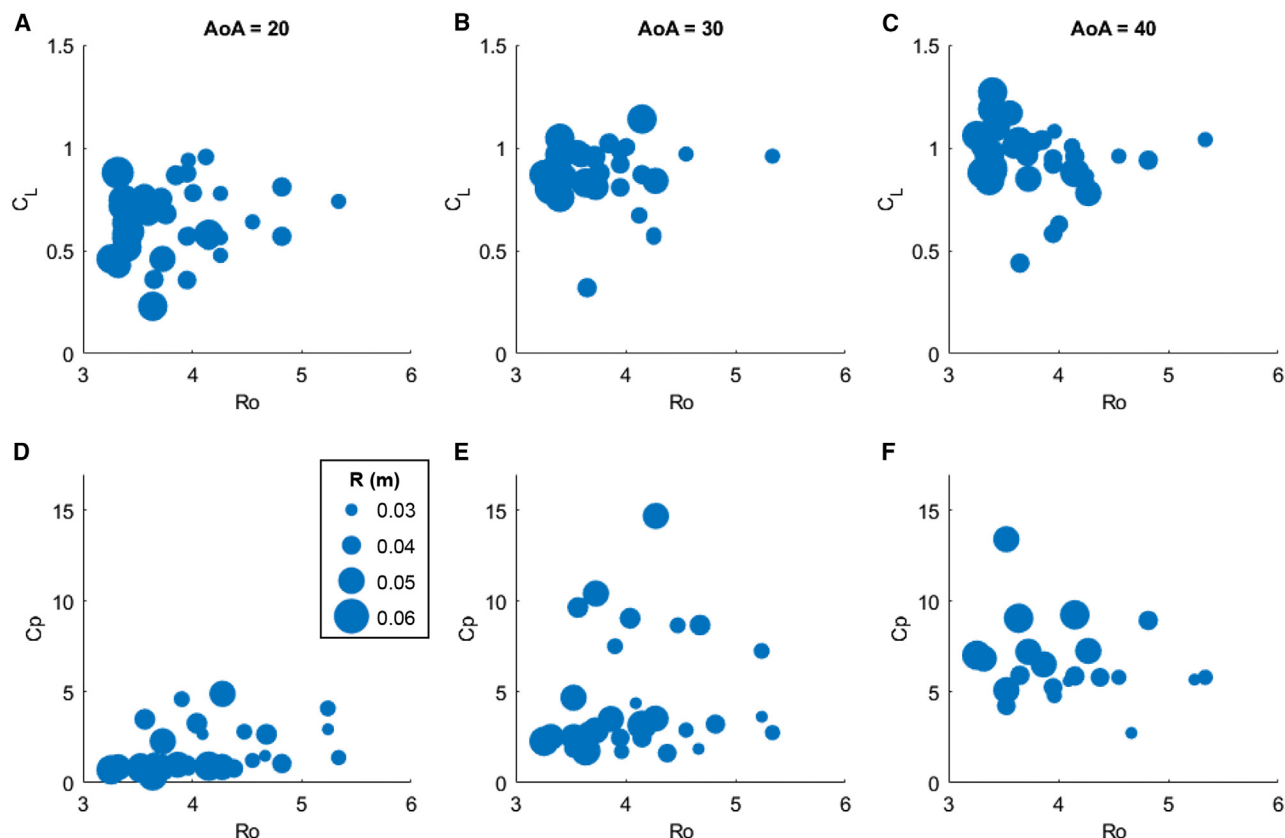
Figure 3. Effect of Rossby number (*Ro*) on the lift coefficient (*C_L*) and input power coefficient (*C_P*) of real beetle wings differing in size (*R* = wing length [m], circle size)

(A–C) Lift coefficient for AoA 20°, 30°, and 40°, respectively. The data are comprised of measurements on 25 different wing pairs ($0.035 \leq R \leq 0.057$ m) and different offsets ($0.02 \leq r \leq 0.036$ m).

(D-F) Input power coefficient for AoA 20°, 30°, and 40°, respectively. C_P is calculated from the electrical power needed to rotate the wings (See STAR Methods section). The data are comprised of measurements on 10 different wing pairs ($0.03 \leq R \leq 0.055$ m) with varying offsets ($0.02 \leq r \leq 0.036$ m).

effect of geometry but overlooking flexibility as a key adaptation of insect wings for improving flight performance.

The mango stem borer (*Batocera rufomaculata*) is a large beetle with extreme intraspecific variance in adult body size (Figure 1A), with populations spanning up to a 7-fold difference in body mass.[51–53] Laboratory studies have shown that this beetle is capable of prolonged flight, exceeding 40 min in some cases, with smaller conspecifics capable of flying longer distances compared to larger ones.[51] Wing length and area in this species scale with body mass to the 0.33 and 0.67 power, respectively, as expected based on geometrical similarity. Accordingly, wing length varies between ∼3 and ∼6 cm in the smallest and largest beetles with many intermediate sizes. The aspect ratio (*AR*, wing length/mean chord) of the wings and their shape (non-dimensional radius of the second moment of area, $\hat{r}_2$[54] do not vary with body mass. Consequently, the planform area of the wings in larger beetles is a magnification of the wings of smaller ones, raising the following question: do small and large wings differ in aerodynamic performance in a manner that helps to explain the ability of smaller beetles to fly longer distances? To address this question, we detached wings from conspecifics differing in size and tested their aero-

dynamic performance in a revolving wing set-up, taking into account the above-mentioned effect of the *Ro* number on the results. Since the results indicated that wing flexibility had an important role in the scaling of aerodynamic performance, we tested the scaling of this flexibility with wing size both statically and dynamically. The results shed new light on the role of flexibility in tuning the scaling of aerodynamic performance in insect wings.

We hypothesized that insect wing flexibility is tuned to passively control the flow separation that is expected to occur in rigid wings at high AoAs and that this tuning corresponds with wing size to mitigate the adverse effect of increasing *Ro* number in smaller revolving wings (Figures 1B and 1C). We suggest that chordwise elastic wing deformations due to aerodynamic loads can morph the wing to change the local AoA and/or camber of the chord, thus improving flow attachment and sustained LEV.[55] It is further suggested that small flexible wings operating at a larger *Ro* number can achieve similar aerodynamic performances to those of larger ones through proportionally larger deformations across the wing planform, thus mitigating the flow separation associated with increased *Ro* number in rigid wings. We suggest that this mechanism can
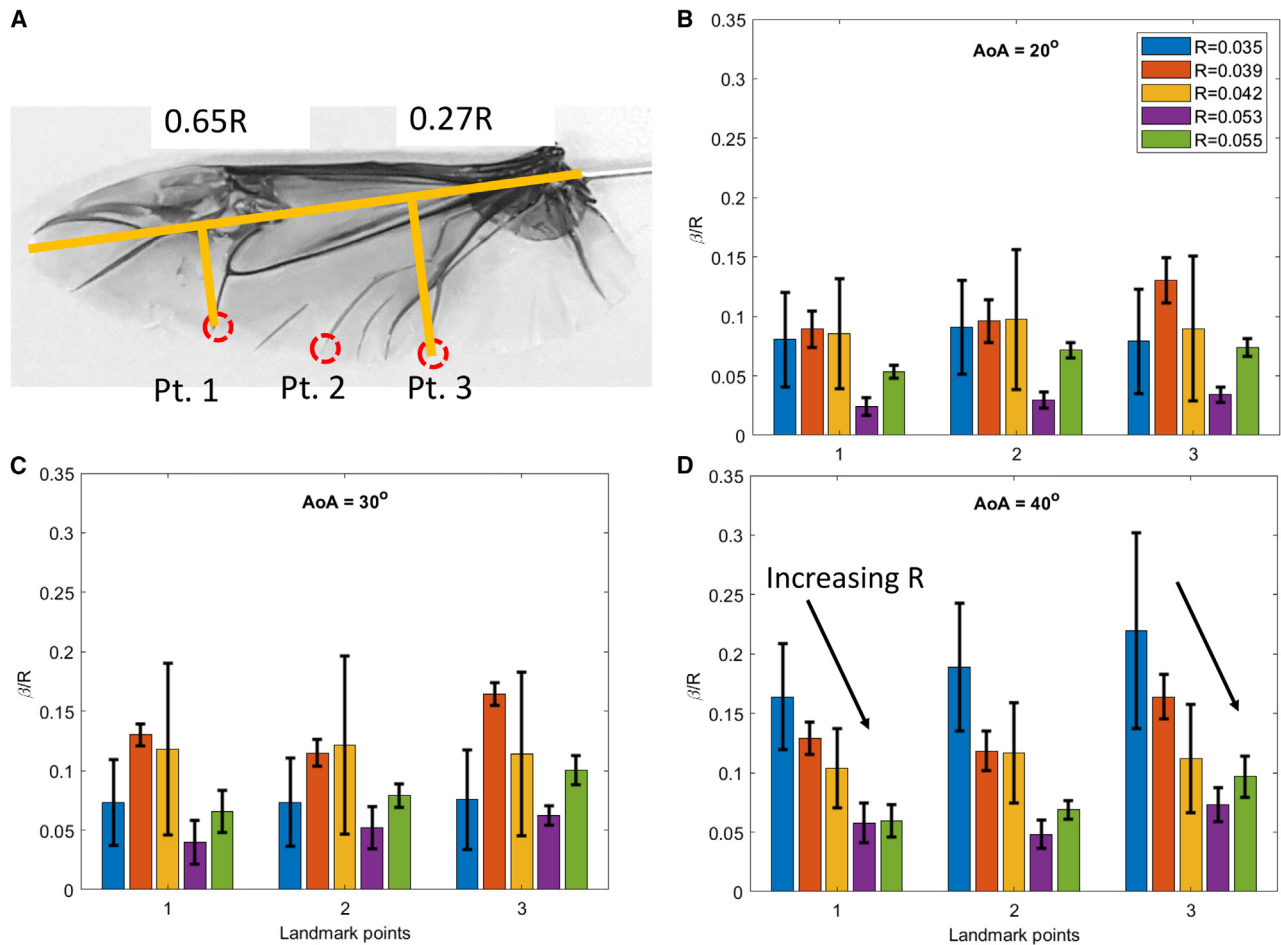
A

0.65R   0.27R

Pt. 1   Pt. 2   Pt. 3

Figure 4. Trailing-edge deflections of revolving wings due to aerodynamic loads
(A) The position of points 1–3 on the trailing edge where the deflections were measured from high-speed movies. Orange lines depict the spanwise positions of points 1 and 3.
(B–D) The deflection of the three points from their expected position on a rigid wing for wings varying in size (R [m], colors) at AoA = 20° (B), 30° (C), and 40° (D). The measured deflection (β) of the points in each wing is normalized by the wing length (β/R). Bars are the means of 2–6 measurements from each of two wings per wing length (R, except for R = 0.039 m that is based on repeated measurements on a single wing due to its pair being damaged). Error bars are the standard error of all measurement per wing size.

also be extended to intraspecific scaling of forward flight in insects based on the following reasoning:

During hovering, the wing speed of revolving and root-flapping wings is coupled with the wing length, since larger wings achieve higher wing-tip speeds for the same flapping frequency (Figure 1B). Smaller insects typically flap at higher frequency than larger ones[56] to compensate for the decrease in wing-tip speed of their shorter wings. This implies a steeper velocity gradient over the smaller wing length (Figure 1C). Insects do not have an anatomical offset (r) between the wing and its hinge. Consequently, during hovering their Ro is equivalent to the AR and does not change with wing size.

During forward flight, most of the lift is generated during the downstroke and the free-stream velocity is redistributed to the spanwise gradient of streamwise velocity shed to the wake. This advance ratio effect leads to the wing root experiencing non-zero flow speeds. This condition is shared with

the revolving wings with an offset distance (r) between the rotation axis and the anatomical wing hinge (Figure 1B). Therefore, the Ro number is to some degree analogous and proportional to the advance ratio, J (see Figure 1 and Data S1) so that a larger J is equivalent to a higher Ro number, at which LEV formation presumably will be compromised. Indeed, J is known to affect the relationship between the lift coefficient and the AoA in rigid revolving wings.[49] Figures 1D and 1E depict two theoretical examples demonstrating that differences in spanwise flow gradients over small and large beetle wings can exist despite similarity in Ro number and J. The two beetles can be flying at the same flight and wing-tip speed (Figure 1D) or the smaller beetle may fly at lower flight and wing-tip speeds (Figure 1E). In both cases, the spanwise velocity gradient remains steeper for the smaller insects regardless of the similarity in J. In the revolving wing equivalent, the spanwise velocity gradient is steeper in smaller revolving wings even if the offset (r) is adjusted to rotate
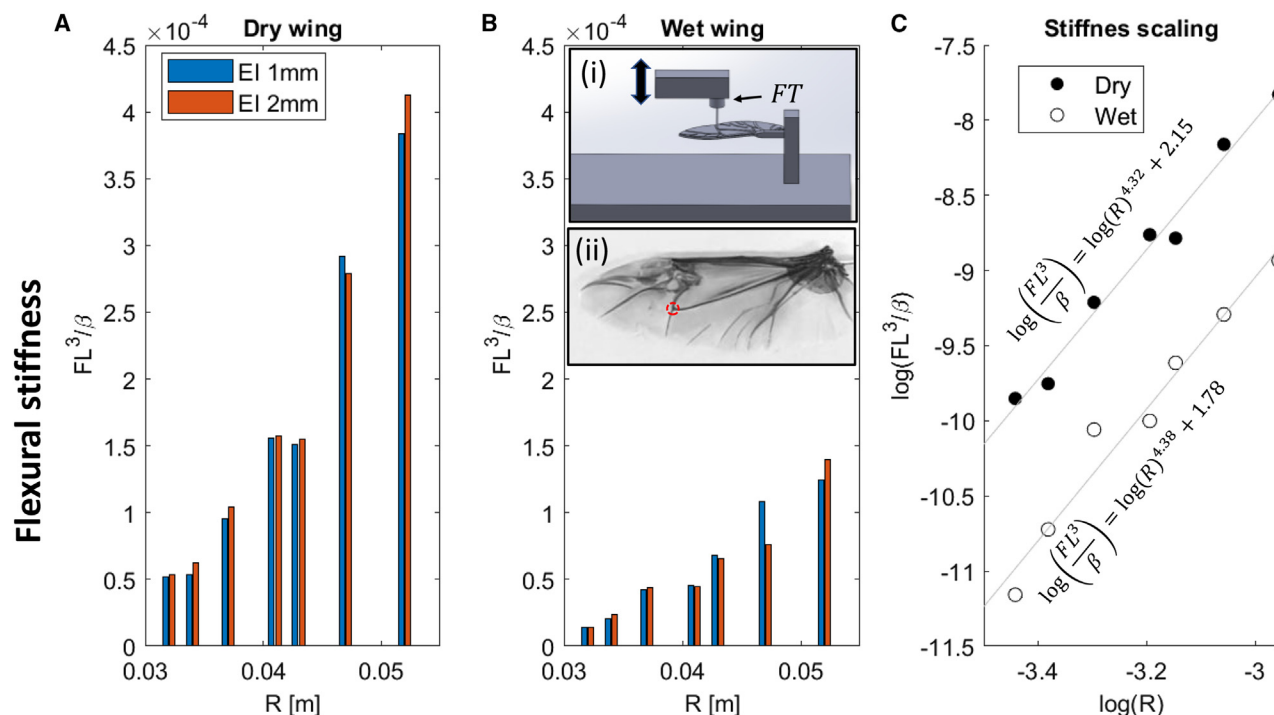
Figure 5. Static bending tests of real beetle wings differing in wing size (*R*)

(A) The flexural stiffness of detached beetle wings measured from the force (F) required to deflect the wing by β = 1 mm (blue bars) and 2 mm (red bars) at a distance L from the support (hinge).

(B) As in (A) but after soaking the wings in water for 24 h. The two inserts in (B) show the static bending method (Bi) and position on the wing (red circle) where the measurements were performed (Bii).

(C) The scaling of flexural stiffness with wing length in the dry and soaked wings. Both linear relationships of the log-transformed data are statistically significant (p≪0.001, $R^2 > 0.96$). Data are based on seven wings differing in size. Each wing was measured twice, for each displacement (1, 2 mm). The bars in (A) and (B) are the average of the two measurements.

both wings at the same *Ro* number (Figures 1D and 1E). This implies that the spanwise distribution of loads on the small and large wings need not be the same despite the dimensional similarity of flapping/revolving flight. How this difference in spanwise velocity distribution translates to aerodynamic performance in revolving wings or forward flight in small and large beetles currently remains unknown. Here, we tested the hypothesis that small beetles have tuned their flexible wings to alter the relationship between the *Ro* number (or *J*) and the C_L such that they avoid the penalty of flying at higher *Ro* numbers during forward flight.

Results and discussion section below describes the experiments where aerodynamic performance as a function of wing size and Ro number section compares the aerodynamic performance of revolving real beetle wings of different sizes with rigid three-dimensional (3D)-printed wings of similar shape and size. The scaling of wing flexibility section tests the scaling of mechanical properties (flexural stiffness) and structural deformations of real beetle wings during revolution (dynamic) and in response to static normal force loading. Wing-veins cross-section section focuses on the cross-section of the wing-veins' structure. Wing-fluid interaction section describes the fluid-wing interaction (at the downwash region) for the real flexible beetle wing using PIV. The main conclusions combined from all

the experiments are presented in conclusions section, followed by details of the extended methodology.

RESULTS AND DISCUSSION

Aerodynamic performance as a function of wing size and Ro number

We tested 3D-printed rigid wings (3.0 ≤ *R* ≤ 6.5 cm) with a uniform offset (*r* = 2.5 cm) and the same planform shape as that of *B. rufomaculata* wings (Figure S1) rotating at a wing-tip speed $U_{tip} = 10$ ms^{-1}. Their C_L displayed the expected increase with AoA (Figure 2A) but also the expected reduction in C_L with increasing *Ro* (decreasing *R*). In contrast, real *B. rufomaculata* wings (3.5 ≤ *R* ≤ 5.7 cm) with the same offset had an overall larger C_L and showed no apparent relationship between the C_L and *R* or *Ro* (Figures 2B and 2C). This suggests that the ability of the smaller wings to avoid the lift reduction penalty associated with an increase in *Ro* is related to the flexibility of real insect wings. To decouple the wing length from the *Ro* number, we repeated the measurements on real beetle wings with larger or smaller offsets (2.0 ≤ *r* ≤ 3.6 cm). The experiment showed that the C_L of real beetle wings did not decrease with *Ro* number (Figures 3A–3C). In lieu of measuring the drag of the wings (or the torque it generated), we measured the electrical power
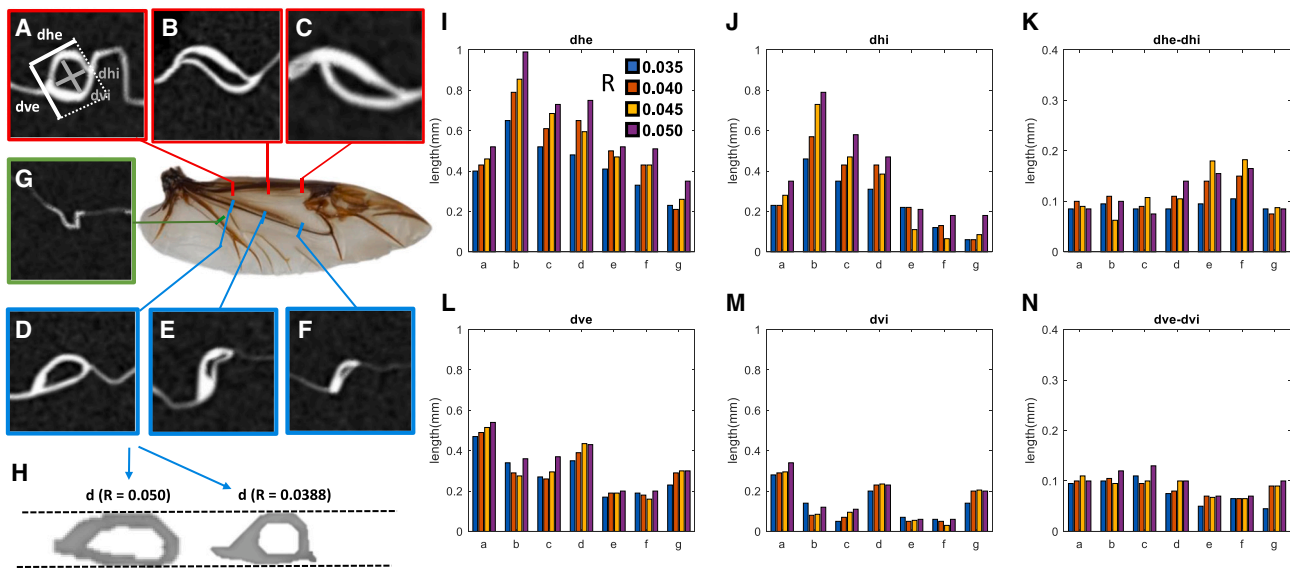
Figure 6. Wing-vein cross-sections from μCT scans

(A–G) Show cross-section of wing veins at the positions marked on the wing image. Color denotes different wing veins. All cross-sections are oriented with the horizontal axes of the image parallel to the wing plane and the vertical axis normal to the wing plane.

(H) Cross-section (D) from a small and a large wing scaled to have the same dve (see A and below), illustrating the difference in cross-section shape between small and large wings.

(I–N) Show the measured diameters and wall thickness of the veins from the scans, where dh_ and dv_ are the diameters oriented in the local membrane plane and normal to it respectively, and the third letter, e or i, (i.e.,: dve, dvi) denotes the external and internal diameters, respectively, as depicted in (A). Color-coded bars in (I–N) correspond to different wing lengths (R, [m]). The measurements were done on two wings from each size category (R), except the R = 0.035 where only a single wing was available. In all other cases the bars are the average of the two wings per wing length.

needed to rotate the wings and found that the non-dimensional power coefficient (C_P) remained independent of Ro as well (Figures 3D–3F). These results are contrary to the expected decrease in C_L (see introduction) and increase in C_P[41] of revolving rigid wings as the Ro number increases. We conclude that real beetle wings are not operating under the same geometrical scaling rule by virtue of their flexibility. Thus, we next sought to explore how this wing flexibility scales with wing size in the real beetle wings and how it adjusts wing shape and flow in the revolving wing set-up.

The scaling of wing flexibility

The elastic deformations of the wings during revolution were measured using two high-speed cameras to extract the deflection in 3D position of three landmarks on the trailing edge.[33] Figure 4 shows these deflections measured from five wing pairs varying in length (3.5 ≤ R ≤ 5.5 cm) as a function of AoA (20°, 30°, 40°). The measured deflection (β) of each wing has been normalized by dividing it by its R. All deflections had the same direction, contributing to twisting and increasing the positive camber of the wings by lowering the trailing edge relative to the leading edge. The normalized wing deformations increased with the AoA due to larger aerodynamic loads. At AoA = 20°, the deflection at the trailing edge was ~3 mm and did not show a specific trend within or across the wings. At AoA = 30°, the normalized deformations of some of the smaller wings appeared to increase more than in the larger wings. At AoA = 40°, a clear trend of relatively lower deformations in the larger

wings became prominent and the deformations within each wing tended to increase from the distal to the more proximal points on the trailing edge (i.e., wing twist).

These results reveal that smaller wings experience proportionally larger deformation compared to larger ones when aerodynamic loads from the wing rotation are applied. The different deformations of the small and large wings could have resulted from differences in the spanwise load distribution on the wing (Figure 1) or from a non-isometric scaling of the mechanical properties with wing length. To test the latter, we tested the scaling of the mechanical properties of the wings by measuring the force needed to bend the wing similar to bending a cantilever beam at a specific location (Figure 5). The wings were secured at the anatomical hinge, and we measured the force required to bend the wing by 1 and 2 mm at the same morphological landmark (Figure 5A). We repeated the experiment after soaking the wings in water for 24 h (Figure 5B) to evaluate how the drying of the detached wings contributed to their flexural stiffness and scaling. The soaked wings had a lower flexural stiffness than the dry ones, but in both cases, stiffness scaled with wing length at scaling exponents (slopes on a log-log plot, Figure 5C) that were statistically indistinguishable (4.32 ± 0.64 versus 4.38 ± 0.98 for the dry and soaked wings, respectively, where the ± values correspond to the 95% confidence interval of each exponent). The scaling of flexural stiffness with the 4.3 power of wing length (dry wings) was significantly higher than the theoretical 3.0 that is expected for a cantilever beam loaded at the tip. It was also significantly higher than the slope
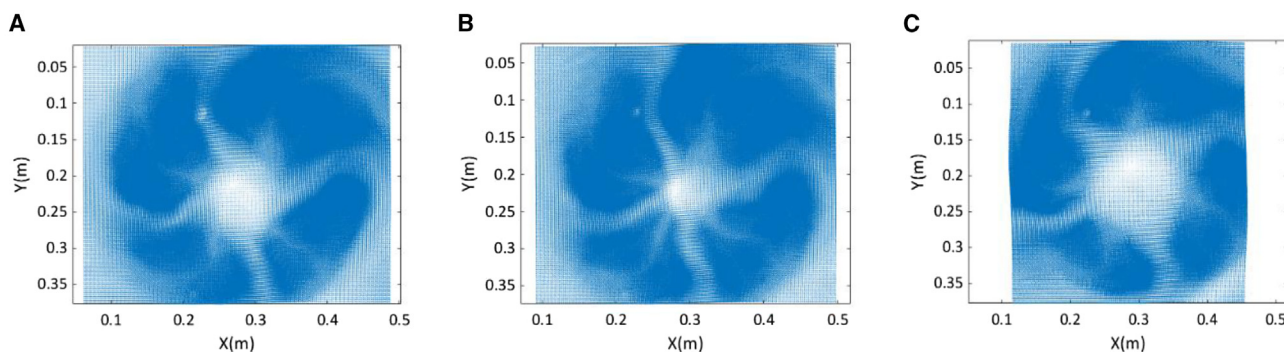
Figure 7. PIV vector maps
Mean velocity maps in the downwash region of a pair of revolving wing (R = 0.045 m, r = 0.025 m) at various AoAs: (A) 20°, (B) 30°, and (C) 40°.

of 2.97 or 2.08 for spanwise and chordwise bending, respectively, obtained interspecifically from 16 insect species from six orders (albeit, no beetles).[32] Thus, the wing stiffness of larger conspecifics of *B. rufomaculata* is greater than that expected based only on increase in wing size. The scaling exponent obtained here does not significantly differ from the 4.0, estimated previously for intraspecific scaling of the chordwise wing stiffness of the beetle *Protaetia cuprea*.[33] It is not clear whether the wing stiffness of beetles scales differently to those of other insects or whether intraspecific scaling of wing stiffness differs substantially from interspecific scaling, in which varying morphologies and flapping kinematics complicate the relationship between wing stiffness and length.

If wing compliance contributes to aerodynamic performance in small revolving wings, and wings soaked in water are more compliant than dry ones, then how does an increase or decrease in compliance affect the aerodynamic performance of the same wing? Wings that were soaked in water for 24 h generated a lower C_L than the same wings prior to soaking, especially at the higher AoA (Figure S2). The soaked wings demonstrated the opposite trend of the *Ro* number effect, with larger wings generating a lower C_L than smaller ones, with this trend diminishing in the dryer wings and becoming similar to that shown in Figure 2C. It seems that the greater stiffness of the larger wings is required for their aerodynamic performance, since higher compliance due to soaking diminished the lift production of the larger wings more than in the smaller ones.

Wing-veins cross-section
The mechanical properties of the wing depend on its material composition, the arrangement of the wing-vein structure, and the cross-section geometry of the veins themselves. To determine whether the latter can explain the proportionally higher stiffness of the larger wings, we scanned wings of various sizes (3.5 < R < 5.0 cm) using μCT and measured the external and internal diameter of three veins at the same locations (Figure 6). We found that the external and internal vein diameters in the wing plane increased with wing length, resulting in both increased vein diameter and wall thickness for the larger wings (Figures 6I–6K). Normal to the wing membrane, both the external and internal diameters showed a slower increase in diameter with wing length and a wall thickness that remained mostly unaf-

fected by wing length (Figures 6L–6N). The differences between the growth of vein diameters in- and out-of-plane led to a cross-section shape change, in which the veins of smaller wings had a more circular cross-section and the same veins of larger wings had an elliptical cross-section with the major axis parallel to the membrane. In transects D–F in Figure 6, however, the major axis that connects the membrane on either side of the vein is rotated so that it is oriented out of the global wing plane. This increase in cross-section diameter and wall thickness on the axis normal to wing planform area can explain the higher stiffness of the larger veins to counteract bending out of the wing plane and the disproportional scaling of this stiffness with wing length relative to an isometric increase in wing size.

Wing-fluid interaction
The flow in the vicinity of flexible beetle wings in the rotating reference frame was studied using 2D PIV. For the intermediate Reynolds number associated with beetle flight (Re < 10^4), one cannot ignore viscous effects coupled with inertia and pressure. The flow structures and turbulence associated with the momentum transfer from the wing motion to the adjunct air, and the energy involved in the generation of this induced flow, determine the aerodynamic performance of the revolving wings. Therefore, we opted to measure the flow beneath the rotating wings. The flow was studied for R = 4.5 cm and r = 2.5 cm, associated with the strong rotational accelerations that presumably stabilize the leading-edge vortex,[37] enhancing lift generation. Figure 7 provides a comprehensive visualization of the velocity field beneath the rotating wings, employing quiver plots for all three AoAs (20°, 30°, 40°). Notably, for all cases, the observed patterns appeared as circular, as previously described.[57] Visually, all three cases exhibit a similar behavior, in which at the core, under the wing offset and hinge, the flow is very slow, approaching a stagnation level and increasing outward from the center. The ray-like patterns are the result of the two rotating wings, such that at every rotation each wing leaves a wake behind it with a lag of the following wing moving in the same direction. The region of low velocity at the center seems to be dependent on the AoA. At 30°, this area is smaller compared to at both 20° and 40°, whereas at 40° it appears to expand more than at 20° (Figure 7). This trend, which also appears in other flow properties, suggests that at ~30° the flow experience

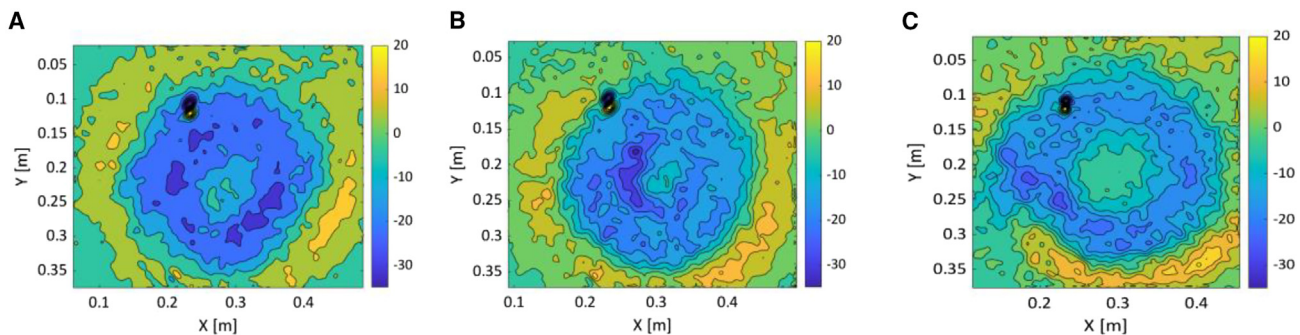**Figure 8. The vorticity field beneath the revoloving wing**
Contours of the mean normal vorticity ($\overline{\omega}_z$) component at the downwash region at various AoAs: (A) 20°, (B) 30°, and (C) 40°.

changes, and at 40° it changes back to the characteristics displayed at lower angles.

To estimate the normal vorticity (ω_z) component from the mean velocity fields, a second-order least squared method was used.[58] Figure 8 depicts the average normal vorticity ($\overline{\omega}_z$) from the 500 maps for each AoA. The ω_z provides an indication of the downwash motion.[59] Commonly, vortices generated by an airfoil, i.e., tip vortices, are associated with lift generation; thus vorticity can serve as an indication to the downwash region.[60] A stronger ω_z suggests an elevated vertical momentum (downwash) and, consequently, increased lift generation. Similar to the mean velocity, a rotational pattern is observed for all AoAs. Here, positive and negative rotational patterns are consistent over the range of AoAs, indicating a strong circular pattern (i.e., "vortex ring") formed beneath the rotating wings. At 20°, the magnitude of vorticity is higher compared to the other two AoAs, suggesting a stronger rotational motion. The weaker motion at 30° and 40° suggests that the flow may experience separation, causing less momentum to transfer in the downwash direction. Here again, the center of rotation is small in terms of area at 30° compared to that at the other angles. The mean vorticity, which is a velocity gradient invariant of the coordinate system, follows a similar trend to that of the mean velocity.

The rotational motion of the wings increases the rate of mixing within the flow. At intermediate Reynolds numbers, the rotational energy increases unsteadiness, shear, and mixing, thus forming turbulence conditions. We applied the classical Reynolds decomposition to estimate several of the turbulence quantities in order to shed light on the coupling effects generated between the flexible wings and the near wake (in the downwash region). We focused on enstrophy (ω'^2, where $\omega' = \omega - \overline{\omega}$), which is associated with the small turbulent scales and is used to indicate turbulence activity.[61] Enstrophy evolution is influenced by the interplay of strain rate, rotation rate, and viscous dissipation. These interactions often display 3D characteristics not directly evident in velocity or vorticity fields.[62] Enstrophy may indicate, especially in shear-free flows, a favorable interaction between the rate of strain and rate of rotation, resulting in the generation of enstrophy, signifying the formation of concentrated vorticity pockets.[63] The normal enstrophy (Figure 9) is a measure of rms of fluctuating vorticity. The enstrophy is significantly higher at AoA = 20° due to increase in shear, which makes it more turbulent and leads to overall increase in enstrophy. At 30° and 40°, the enstrophy levels decrease (see Figure S3), suggesting that the flow over the wing is in some sort of transitional stage, experiencing separation, which causes less momentum in the vertical direction toward the downwash region. The uniform distribution of the enstrophy at 30° compared to at the other AoAs seems to indicate less turbulent activity. One possibility is that at 30° the flow may be in a transitional stage, with the separation zone possibly smaller or the flow not separating at all, which would lead to a more uniform distribution of enstrophy. One would have expected to observe a monotonic decrease in enstrophy with the increase of AoA in rigid wings. However, in these experimental settings, the enstrophy values for 40° are slightly higher than at 30°. This suggests that the wing flexibility coupled with a high AoA alters the flow dynamics in the downwash region in a non-linear fashion. In order to identify coherent vortices in a flow, we applied the swirl ratio method[64] to the PIV data.

Based on the swirl ratio analysis (see Figure S4), we estimated the geometrical parameters of the identified coherent flow patterns: i.e., the diameter of the pattern and its thickness (Table 1). These parameters further support the observation that at 40° the flow changes compared to at 30°, whereas it has presumably already begun to separate at 30°. Although one would expect to observe a trend of continuous decrease in diameter and thickness as the wings move to a higher AoA, the lack of such a trend when moving from AoA 30° to 40° potentially indicates less separation at 40°.

The measured flow beneath the wings generally conforms to the dynamic and static observations on the wing deformations and force measurements (sections "aerodynamic performance as a function of wing size and Ro number" and "the scaling of wing flexibility"). The scaling of wing flexibility section shows that wing deformation increases with the AoA becoming more significant at 40° and thus changing the FSI of the wing at higher AoA. Aerodynamic performance as a function of wing size and Ro number section shows that some transitions in the aerodynamics seem to occur at AoA ∼30°, since C_L was much higher than at 20° but not much lower than at 40°. Reattachment of the flow at higher AoA as a result of increase in wing twist and camber may explain the observed transition in the flow at 30°.
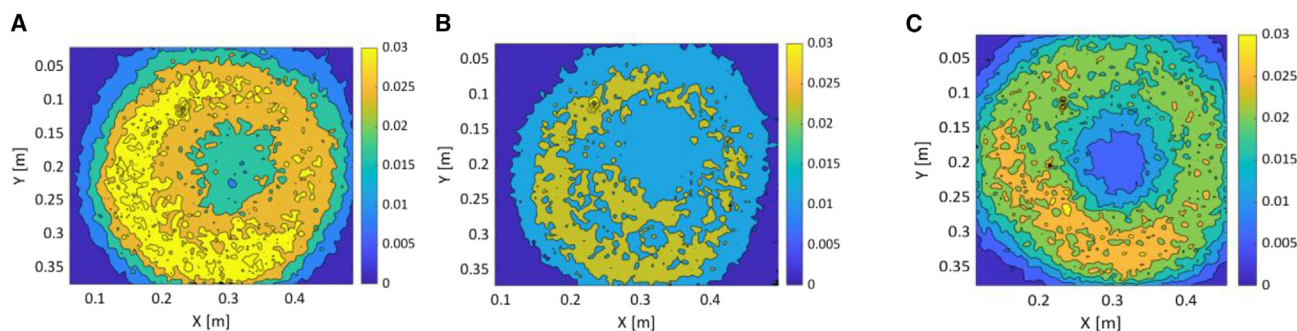
Figure 9. Turbulence characteristic beneath the revolving wing
Contours of the normal enstrophy component ($\overline{\omega_z'^2}$) as a function of AoAs: (A) 20°, (B) 30°, and (C) 40°.

As the additional wake flow properties, such as the 2D turbulent kinetic energy (TKE) and Reynolds stress (RS), did not exhibit any unexpected findings, they are provided in Figures S5 and S6, respectively. Both TKE and RS decreased with AoA, where at the center of rotation TKE/RS are minimal, and at the edge, where shear dominates, they reached maximal values. Their reduction in strength at 30° can be associated with the separation of the flow over the wing, thus providing less momentum in the downwash direction (i.e., reduction in lift without increase in drag).

Conclusions
Our study has shown that flexible *B. rufomaculata* wings avoid the decrease in C_L that occurs with the increase in *Ro* number in rigid wings. This is achieved through wing compliance in the real beetle wings, in which flexural stiffness increases with the increase in wing length faster than would be expected based on geometrical similarity. The mechanism that controls this scaling reflects the anisometric growth of the wing vein diameters, resulting in differences in the wall thickness and the cross-section shape between small and large wings. As a result, smaller wings can experience larger deformations than larger wings under similar flow conditions (i.e., wing-tip speed). These deformations increase with the AoA and become particularly large at AoA ≥ 40° due to the higher aerodynamic loads associated with the large AoA. Although our set-up could not directly describe the FSI associated with the compliance of the wings, the flow observed at the downwash region beneath the wing provides evidence that the wing deformations at AoA >30° maintain the aerodynamic performance of wings at higher AoAs, presumably through the wings passively morphing to retard flow separation. A similar improvement in flow attachment in flexible rectangular wings revolving at large AoA (45°) has been described by van de Meerendonk et al.[55] Noteworthy, wing flexibility in their experi-

ments decreased the effective AoA, whereas here in real beetle wings, it mostly increased wing twist and camber and depended on wing size. Insect wings operate at large AoAs, at which conventional rigid airfoils operating at high Re numbers would stall.[65] Our study demonstrates how flexible insect wings constitute "smart" structures, improving aerodynamic performance by manipulating the complex FSI associated with the flexible wings. This manipulation is achieved passively by the mechanical properties of the wing and therefore does not require control by the nervous system, as demonstrated in our experiments on detached wings.

Limitations of the study
Our report of wing deformations, aerodynamic forces, and flow measurements suggests a passive flow control mechanism that retards, and possibly affix, flow separation from insect wings at high AoA and/or high *Ro* numbers. Corroborating this suggestion requires direct measurement of the flow over the elastic wings, which was not possible in the set-up of the current study. Another open question remaining is to what extent our study on detached *B. rufomaculata* wings applies to insect wings in general? Finally, while our study tested insect wings under angular acceleration and spanwise velocity gradients, the revolving wings set-up does not capture the full complexity of the unsteady flow and FSI in flapping insect wings, leaving ample room for future studies on the relationship between elastic wing deformations and insect flight aerodynamics.

Table 1. Geometrical dimensions of the identified flow patterns at the downwash region extracted through swirl ratio

AoA	Diameter [mm]	Thickness [mm]
20°	36	8
30°	33	6
40°	37	6

AUTHOR CONTRIBUTIONS

Conceptualization, G.R. and R.G.; methodology, G.R., O.S., and R.G.; investigation, O.S., M.R., D.M., K.S., and D.D.-E.; writing—original draft, G.R. and R.G.; writing—review & editing, G.R., R.G., O.S., and K.S.; funding acquisition, G.R. and R.G.; resources, G.R. and R.G.; visualization: O.S., K.S., and D.D.-E.; supervision, G.R. and R.G.

DECLARATION OF INTERESTS

The authors declare no competing interests.

STAR★METHODS

Detailed methods are provided in the online version of this paper and include the following:

- KEY RESOURCES TABLE
- EXPERIMENTAL MODEL AND STUDY PARTICIPANT DETAILS
- METHOD DETAILS
  - Force measurements with variable R and r
  - Static bending tests (dry and soaked wings)
  - Revolving wing deformation test
  - Micro-CT scanning
  - PIV set-up and data analysis
- QUANTIFICATION AND STATISTICAL ANALYSIS

SUPPLEMENTAL INFORMATION

Supplemental information can be found online at https://doi.org/10.1016/j.isci.2025.112035.

REFERENCES

1. Wootton, R. (2020). The geometry and mechanics of insect wing deformations in flight: A modelling approach. Insects *11*, 446. https://doi.org/10.3390/insects11070446.

2. Wootton, R. (1992). Functional morphology of insect wings. Annu. Rev. Entomol. *37*, 113–140.

3. Combes, S.A., and Daniel, T.L. (2003). Into thin air: contributions of aerodynamic and inertial-elastic forces to wing bending in the hawkmoth Manduca sexta. J. Exp. Biol. *206*, 2999–3006. https://doi.org/10.1242/jeb.00502.

4. Phan, H.V., and Park, H.C. (2019). Insect-inspired, Tailless, Hover-Capable Flapping-Wing Robots: Recent Progress, Challenges, and Future Directions at (Elsevier Ltd). https://doi.org/10.1016/j.paerosci.2019.100573.

5. Chen, L., Cheng, C., Zhou, C., Zhang, Y., and Wu, J. (2024). Flapping rotary wing: A novel low-Reynolds number layout merging bionic features into micro rotors. Prog. Aerosp. Sci. *146*, 100984. https://doi.org/10.1016/j.paerosci.2024.100984.

6. Pan, Y., Guo, S., and Huang, X. (2024). Research Progress on Bio-inspired Flapping-Wing Rotor Micro Aerial Vehicle Development. J. Bionic Eng. *21*, 1621–1643. https://doi.org/10.1007/s42235-024-00521-7.

7. Ennos, A.R. (1988). The importance of torsion in the design of insect wings. J. Exp. Biolgy *140*, 137–160. https://doi.org/10.1242/jeb.140.1.137.

8. Ennos, A.R. (1989). Inertial and aerodynamic torques on the wings of diptera in flight. J. Exp. Biolgy *142*, 87–95. https://doi.org/10.1242/jeb.142.1.87.

9. Young, J., Walker, S.M., Bomphrey, R.J., Taylor, G.K., and Thomas, A.L.R. (2009). Details of insect wing design and deformation enhance aerodynamic function and flight efficiency. Science *325*, 1549–1552. https://doi.org/10.1126/science.1175928.

10. Bluman, J., and Kang, C.k. (2017). Achieving hover equilibrium in free flight with a flexible flapping wing. J. Fluids Struct. *75*, 117–139. https://doi.org/10.1016/j.jfluidstructs.2017.08.011.

11. Wang, Q., Goosen, J.F.L., and van Keulen, F. (2017). An efficient fluid–structure interaction model for optimizing twistable flapping wings. J. Fluids Struct. *73*, 82–99. https://doi.org/10.1016/j.jfluidstructs.2017.06.006.

12. Olivier, M., and Dumas, G. (2016). A parametric investigation of the propulsion of 2D chordwise-flexible flapping wings at low Reynolds number using numerical simulations. J. Fluids Struct. *63*, 210–237. https://doi.org/10.1016/j.jfluidstructs.2016.03.010.

13. Ishihara, D., and Onishi, M. (2023). Computational fluid–structure interaction framework for passive feathering and cambering in flapping insect wings. Int. J. Numer. Methods Fluids *96*, 435–481. https://doi.org/10.1002/FLD.5251.

14. Schwab, R., Johnson, E., and Jankauski, M. (2019). A Novel Fluid – Structure Interaction Framework for Flapping , Flexible Wings. J. Vib. Acoust. *141*, 1–13. https://doi.org/10.1115/1.4044268.

15. Fairuz, Z.M., Abdullah, M.Z., Zubair, M., Abdul Mujeebu, M., Abdullah, M.K., Yusoff, H., and Abdul Aziz, M.S. (2016). Effect of wing deformation on the aerodynamic performance of flapping wings : fluid-structure interaction approach. J. Aerosp. Eng. *29*, 04016006. https://doi.org/10.1061/(ASCE)AS.1943-5525.0000548.

16. Hedrick, T.L., Combes, S.A., and Miller, L.A. (2015). Recent developments in the study of insect flight. Can. J. Zool. *93*, 925–943. https://doi.org/10.1139/cjz-2013-0196.

17. Shyy, W., Aono, H., Chimakurthi, S.K., Trizila, P., Kang, C.K., Cesnik, C.E.S., and Liu, H. (2010). Recent progress in flapping wing aerodynamics and aeroelasticity. Prog. Aerosp. Sci. *46*, 284–327. https://doi.org/10.1016/j.paerosci.2010.01.001.

18. Song, F., Yan, Y., and Sun, J. (2023). Review of insect-inspired wing micro air vehicle. Arthropod Struct. Dev. *72*, 101225. https://doi.org/10.1016/J.ASD.2022.101225.

19. Mountcastle, A.M., and Combes, S.A. (2013). Wing flexibility enhances load-lifting capacity in bumblebees. Proc. Biol. Sci. *280*, 20130531. https://doi.org/10.1098/rspb.2013.0531.

20. Du, G., and Sun, M. (2010). Effects of wing deformation on aerodynamic forces in hovering hoverflies. J. Exp. Biol. *213*, 2273–2283. https://doi.org/10.1242/jeb.040295.

21. Shoele, K., and Zhu, Q. (2013). Performance of a wing with nonuniform flexibility in hovering flight. Phys. Fluids *25*, 041901. https://doi.org/10.1063/1.4802193.

22. Nakata, T., and Liu, H. (2012). Aerodynamic performance of a hovering hawkmoth with flexible wings: a computational approach. Proc. Biol. Sci. *279*, 722–731. https://doi.org/10.1098/rspb.2011.1023.

23. Vanella, M., Fitzgerald, T., Preidikman, S., Balaras, E., and Balachandran, B. (2009). Influence of flexibility on the aerodynamic performance of a hovering wing. J. Exp. Biol. *212*, 95–105. https://doi.org/10.1242/jeb.016428.

24. Jankauski, M., Guo, Z., and Shen, I.Y. (2018). The effect of structural deformation on flapping wing energetics. J. Sound Vib. *429*, 176–192. https://doi.org/10.1016/j.jsv.2018.05.005.

25. Tanaka, H., Whitney, J.P., and Wood, R.J. (2011). Effect of flexural and torsional wing flexibility on lift generation in hoverfly flight. Integr. Comp. Biol. *51*, 142–150. https://doi.org/10.1093/icb/icr051.

26. Zhao, L., Huang, Q., Deng, X., and Sane, S.P. (2010). Aerodynamic effects of flexibility in flapping wings. J. R. Soc. Interface 7, 485–497. https://doi.org/10.1098/rsif.2009.0200.

27. Tobing, S., Young, J., and Lai, J. (2017). Effects of wing flexibility on bumblebee propulsion. J. Fluids Struct. 68, 141–157. https://doi.org/10.1016/j.jfluidstructs.2016.10.005.

28. Chen, L., Yang, F.L., and Wang, Y.Q. (2022). Analysis of nonlinear aerodynamic performance and passive deformation of a flexible flapping wing in hover flight. J. Fluids Struct. 108, 103458. https://doi.org/10.1016/J.JFLUIDSTRUCTS.2021.103458.

29. Shahzad, A., Tian, F.B., Young, J., and Lai, J.C.S. (2017). Numerical study of rigid and flexible wing shapes in hover. J. Phys, Conf. Ser. 822, 012007. https://doi.org/10.1088/1742-6596/755/1/011001.

30. Shahzad, A., Tian, F.B., Young, J., and Lai, J.C. (2018). Effects of flexibility on the hovering performance of flapping wings with different shapes and aspect ratios. J. Fluids Struct. 81, 69–96. https://doi.org/10.1016/j.jfluidstructs.2018.04.019.

31. Wang, L., and Wu, T. (2021). Effect of Wing Flexibility on the Lift Force Generated by a 2D Model Insect Wing Flapping in Hover Mode. Int. J. Appl. Mech. 13, 2150056. https://doi.org/10.1142/S1758825121500563.

32. Combes, S.A., and Daniel, T.L. (2003). Flexural stiffness in insect wings I. Scaling and the influence of wing venation. J. Exp. Biol. 206, 2979–2987. https://doi.org/10.1242/jeb.00523.

33. Meresman, Y., and Ribak, G. (2017). Allometry of wing twist and camber in a flower chafer during free flight: How do wing deformations scale with body size? R. Soc. Open Sci. 4, 171152. https://doi.org/10.1098/rsos.171152.

34. Chen, L., and Wu, J. (2024). Coexistence of dual wing–wake interaction mechanisms during the rapid rotation of flapping wings. J. Fluid Mech. 987, A16. https://doi.org/10.1017/JFM.2024.391.

35. Dickinson, M.H., Lehmann, F.O., and Sane, S.P. (1999). Wing rotation and the aerodynamic basis of insect right. Science 284, 1954–1960. https://doi.org/10.1126/science.284.5422.1954.

36. Usherwood, J.R., and Ellington, C.P. (2002). The aerodynamics of revolving wings I. Model hawkmoth wings. J. Exp. Biol. 205, 1547–1564. https://doi.org/10.1242/jeb.205.11.1547.

37. Lentink, D., and Dickinson, M.H. (2009). Rotational accelerations stabilize leading edge vortices on revolving fly wings. J. Exp. Biol. 212, 2705–2719. https://doi.org/10.1242/jeb.022269.

38. Chen, L., Cheng, B., and Wu, J. (2023). Vorticity dynamics and stability of the leading-edge vortex on revolving wings. Phys. Fluids 35, 91301. https://doi.org/10.1063/5.0160346/2909342.

39. Chen, L., Wang, L., Zhou, C., Wu, J., and Cheng, B. (2022). Effects of Reynolds number on leading-edge vortex formation dynamics and stability in revolving wings. J. Fluid Mech. 931, A13–A23. https://doi.org/10.1017/jfm.2021.950.

40. Chen, L., Zhou, C., Werner, N.H., Cheng, B., and Wu, J. (2023). Dual-stage radial-tangential vortex tilting reverses radial vorticity and contributes to leading-edge vortex stability on revolving wings. J. Fluid Mech. 963, 1–25. https://doi.org/10.1017/jfm.2023.196.

41. Kruyt, J.W., van Heijst, G.F., Altshuler, D.L., Lentink, D., Kruyt, J.W., Van Heijst, G.F.J.F., and Altshuler, D.L. (2015). Power reduction and the radial limit of stall delay in revolving wings of different aspect ratio. J. R. Soc. Interface 12, 20150051. https://doi.org/10.1098/RSIF.2015.0051.

42. Lee, Y.J., Lua, K.B., and Lim, T.T. (2016). Aspect ratio effects on revolving wings with Rossby number consideration. Bioinspir. Biomim. 11, 056013. https://doi.org/10.1088/1748-3190/11/5/056013.

43. Carr, Z.R., Devoria, A.C., and Ringuette, M.J. (2015). Aspect-ratio effects on rotating wings: Circulation and forces. J. Fluid Mech. 767, 497–525. https://doi.org/10.1017/jfm.2015.44.

44. Jardin, T., and Colonius, T. (2018). On the lift-optimal aspect ratio of a revolving wing at low Reynolds number. J. R. Soc. Interface 15, 20170933. https://doi.org/10.1242/jeb.022269.

45. Garmann, D.J., and Visbal, M.R. (2014). Dynamics of revolving wings for various aspect ratios. J. Fluid Mech. 748, 932–956. https://doi.org/10.1017/jfm.2014.212.

46. Bhat, S.S., Zhao, J., Sheridan, J., Hourigan, K., and Thompson, M.C. (2019). Uncoupling the effects of aspect ratio , Reynolds number and Rossby number on a rotating insect-wing planform. J. Fluid Mech. 859, 921–948. https://doi.org/10.1017/jfm.2018.833.

47. Bhat, S.S., Zhao, J., Sheridan, J., Hourigan, K., and Thompson, M.C. (2018). The leading-edge vortex on a rotating wing changes markedly beyond a certain central body size. R. Soc. Open Sci. 5, 172197. https://doi.org/10.1098/rsos.172197.

48. Harbig, R.R., Sheridan, J., and Thompson, M.C. (2013). Reynolds number and aspect ratio effects on the leading-edge vortex for rotating insect wing planforms. J. Fluid Mech. 717, 166–192. https://doi.org/10.1017/jfm.2012.565.

49. Dickson, W.B., and Dickinson, M.H. (2004). The effect of advance ratio on the aerodynamics of revolving wings. J. Exp. Biol. 207, 4269–4281. https://doi.org/10.1242/jeb.01266.

50. Ellington, C.P. (1984). The Aerodynamics of hovering insect flight. I. The quasi-steady analysis. Philos. Trans. R. Soc. B 305, 1–15. https://doi.org/10.1098/rstb.1984.0049.

51. Brown, S., Soroker, V., and Ribak, G. (2017). Effect of larval growth conditions on adult body mass and long-distance flight endurance in a wood-boring beetle: Do smaller beetles fly better? J. Insect Physiol. 98, 327–335. https://doi.org/10.1016/j.jinsphys.2017.02.008.

52. Urca, T., and Ribak, G. (2021). The relationship between body size and flight power output in the mango stem borer (Batocera rufomaculata). J. Insect Physiol. 133, 104290. https://doi.org/10.1016/j.jinsphys.2021.104290.

53. Urca, T., Levin, E., Gefen, E., and Ribak, G. (2024). Intraspecific scaling and early life history determine the cost of free-flight in a large beetle (Batocera rufomaculata). Insect Sci. 31, 524–532. https://doi.org/10.1111/1744-7917.13250.

54. Ellington, C.P. (1984). The aerodynamics of hovering insect flight. II. Morphological parameters. Philos. Trans. R. Soc. B 305, 17–40. https://doi.org/10.1098/rstb.1984.0050.

55. van de Meerendonk, R., Percin, M., and van Oudheusden, B.W. (2018). Three-dimensional flow and load characteristics of flexible revolving wings. Exp. Fluids 59, 161–222. https://doi.org/10.1007/s00348-018-2613-1.

56. Dudley, R. (2000). The Biomechanics of Insect Flight (Princeton University Press).

57. Hopfinger, E., and Van Heijst, G.J.F. (1993). Vortices in rotating fluids. Annu. Rev. Fluid Mech. 25, 241–289. https://www.annualreviews.org/doi/pdf/10.1146/annurev.fl.25.010193.001325.

58. Raffel, M., Willert, C., and Kompenhans, J. (1998). Particle Image Velocimetry: A Practical Guide (Springer).

59. Kirchhefer, A.J., Kopp, G.A., and Gurka, R. (2013). The near wake of a freely flying European starling. Phys. Fluids 25, 051902. https://doi.org/10.1063/1.4807064.

60. Saffman, P.G. (1995). Vortex Dynamics (Cambridge Press).

61. Tsinober, A. (2001). An Informal Introduction to Turbulence, 63 (Springer-Nature). https://doi.org/10.1007/0-306-48384-X.

62. Goli, S., Roy, A., and Roy, S. (2019). Vortex filamentation and fragmentation phenomena in flapping motion and effect of aspect ratio and frequency on global strain, rotation, and enstrophy. Int. J. Micro Air Veh. 11, 1756829319836268. https://doi.org/10.1177/1756829319836268.

63. Gurka, R., Liberzon, A., and Hetsroni, G. (2006). POD of vorticity fields: A method for spatial characterization of coherent structures. Int. J. Heat Fluid Flow 27, 416–423. https://doi.org/10.1016/J.IJHEATFLUIDFLOW.2006.01.001.

64. Zhou, J., Adrian, R.J., Balachandar, S., and Kendall, T.M. (1999). Mechanisms for generating coherent packets of hairpin vortices in channel flow.

J. Fluid Mech. *387*, 353–396. https://doi.org/10.1017/S002211209900467X.

65. Sane, S.P. (2003). The aerodynamics of insect flight. J. Exp. Biol. *206*, 4191–4208. https://doi.org/10.1242/jeb.00663.

66. Hedrick, T.L. (2008). Software techniques for two- and three-dimensional kinematic measurements of biological and biomimetic systems. Bioinspir. Biomim. *3*, 034001. https://doi.org/10.1088/1748-3182/3/3/034001.

67. Ribak, G., Pitts, M.L., Wilkinson, G.S., and Swallow, J.G. (2009). Wing shape , wing size , and sexual dimorphism in eye-span in stalk-eyed flies (Diopsidae). Biol. J. Linn. Soc. *98*, 860–871. https://doi.org/10.1111/j.1095-8312.2009.01326.x.

68. Meresman, Y., Husak, J.F., Ben-Shlomo, R., and Ribak, G. (2020). Morphological diversification has led to inter-specific variation in elastic wing defor-mation during flight in scarab beetles. R. Soc. Open Sci. *7*, 200277. https://doi.org/10.1098/rsos.200277.

69. Mountcastle, A.M., and Daniel, T.L. (2009). Aerodynamic and functional consequences of wing compliance. Exp. Fluids *46*, 873–882. https://doi.org/10.1007/s00348-008-0607-0.

70. Weis-Fogh, T. (1973). Quick estimates of flight fitness in hovering animals including novel mechanisms for lift production. J. Exp. Biol. *59*, 169–230. https://doi.org/10.1242/jeb.59.1.169.

71. Jensen, M. (1956). Biology and physics of locust flight. III. The aerodynamics of locust flight. Philos. Trans. R. Soc. B *239*, 511–552. https://doi.org/10.1098/rstb.1956.0009.

STAR★METHODS

KEY RESOURCES TABLE

REAGENT or RESOURCE	SOURCE	IDENTIFIER
Experimental models: Organisms/strains		
Batocera rufomaculata	Lab Reared	NA
Software and algorithms		
MATLAB codes DLTdv5 and Easy wand5	Hedrick[66]	https://biomech.web.unc.edu/dltdv/
Dragonfly	Comet Group	https://dragonfly.comet.tech/en/product-overview/dragonfly-3d-world
Deposited data		
PIV vector maps		https://ci.coastal.edu/

EXPERIMENTAL MODEL AND STUDY PARTICIPANT DETAILS

Research model: The study uses wings of the beetle *Batocera rufomaculata. Developmental stage*: Imago, the wings were removed from dead adult beetles. *Sex*: The current study makes no distinction between wings taken from male or female beetles since previous work in the lab compared the flight and wings of males and females and found no significant inter-sex differences. Similarly, *B. rufomaculata* displays high intraspecific variance in adult body mass but the body mass ranges of males and females overlap. *Population maintenance and care*: the beetles were taken from a population maintained at Tel Aviv University. The animals in the population are individually housed in 1 L glass jars with fresh fig tree twigs for food. Rearing temperature is maintained at $27° ± 2°$. *Allocation to experiments:* The wings available for the study were sorted by their length and then randomly allocated to the different experiments to represent a wide range of wing sizes for each experiment.

METHOD DETAILS

Force measurements with variable R and r

The revolving wing set-up (Figure 2A) comprised a DC motor connected to an electric power source. Controlling the voltage supplied by the power source controlled the rotation rate of the motor. The shaft of the motor was oriented vertically with a horizontal connector mounted on its tip. The two horizontal arms of the connector spanned 5 cm. The rigid 3D-printed wings, R = {3.0, 4.5, 5.0, 6.5 cm}, with the planform shape of the beetle wings (Figure S1) were printed together with the connector in six copies each at a different AoA (0°, 10°, 20°, 30°, 40° and 50°). For the real beetle wing we used the same 3D printed connector but with two holes (4 mm apart) drilled at its ends, to which the two ends of a U-shaped metal pole (diameter = 1 mm) could be fitted. *B. rufomaculata* wings of various sizes and including the wing hinge were carefully removed from dead beetles. The folded wings were spread open and placed between two transparencies, which were sealed with tape to minimize water loss prior to measurements. For the measurements, we removed the wings from the transparencies and glued each one at its root to the U-shaped metal pole. Fitting the ends of the pole into the connector ensured that the length of the wings on either side of the connector was parallel to the ground. We switched between 6 different connectors that were identical in shape and mass except for the orientation of the two holes mounting the wings at different AoA. The motor was then activated to rotate the wings at a given AoA, about the vertical axis (i.e., in a horizontal plane). The motor with the wings was mounted on top of a load cell (LB9H, Zimech) measuring the force in the vertical axis at 100 Hz. When the motor was off, the load cell measured the weight of the entire apparatus. When the motor was on, the revolving wings generated a vertical aerodynamic force (lift) which was registered by the load cell as a reduction in the weight of the motor + wings, enabling extraction of the mean lift using the known mass of the apparatus. We used a high-speed camera filming at 1,000 frames per second to measure the revolution rate of the revolving wings. We adjusted the revolution rate according to the wing length (R) and offset distance (r) to retain the same wing-tip speed. The Rossby number for each trial was calculated as in Lee et al. (2016):

$$Ro = \frac{R_2}{\bar{c}}$$

where R_2 is the second radius of gyration of the beetle wing while accounting for the offset r, and $\bar{c}$ is the mean wing chord. Both R_2 and $\bar{c}$ were extracted from the digital images of the wings' contour as described in Ribak et al.[67] The instantaneous lift measurements were averaged over time, and from the mean lift ($\bar{L}$) we found the lift coefficient C_L for a given AoA as in Usherwood and Ellington[36] and introduction section. We subtracted the C_L measured at AoA = 0° from the measurements at higher AoA in the same wing pairs to correct for any vertical force associated with the revolving connector or small bias in gluing the different wings. Note that Usherwood and Ellington[36] made a more accurate distinction between the measured vertical force and wing lift by accounting for the effect of

downwash velocity on the aerodynamic AoA of a wing blade. Here, we do not make this distinction and use only the geometrical AoA at the wing root, thus referring to vertical aerodynamic force as lift.

In total, we carried out the lift measurements on 20 beetle wing pairs ($3.0 \leq R \leq 5.7$ cm) and the four 3D-printed rigid wings in a range of AoA of $0°$-$50°$. The offset was $r=2.5$ cm and the wing-tip speed was 10 ms^{-1} in all of these measurements.

In a different set of measurements, we varied the offsets $r = \{2.2, 2.8, 3.6$ cm$\}$ used on the same four wing pairs to change Ro without changing wing length. In parallel with some of the measurement, a reading of the current (I) and voltage (V) supplied to the motor by the power source provided the input electrical power ($P_{in} = I \cdot V$) required to rotate the wings at the desired speed. The non-dimensional input power coefficient (C_P) was calculated from P_{in} for a given AoA as:

$$C_P = \frac{2P_{in}}{\rho S_3 \Omega^3}$$

where S_3 is the third moment of wing area of the wing pair that includes the offset r. The C_P measurements were performed on 10 wing pairs ($3.0 \leq R \leq 5.4$ cm) and 6 offsets $r = \{2.0, 2.2, 2.5, 2.8, 3.0, 3.6$ cm$\}$ for the same AoA range. The wing tip speed in these experiments of variable r (Figure 3) was set at 7 ms^{-1}.

Static bending tests (dry and soaked wings)

The scaling of flexural stiffness in real beetle wings was measured on detached wings $R = \{3.2, 3.4, 3.7, 4.1, 4.3, 4.7, 5.2$ cm$\}$ glued at their root to the edge of glass microscope slide. We used acrylic glue mixed with baking soda to ensure that the root was encased from all sides and the wing protruded from the edge of the slide horizontally as a cantilever beam. We measured the force required to bend the wing by pressing normal to the wing plane at a specific vein junction (located at 0.62R, Fig. 5Bii) to displace it by 1 and 2 mm, using a needle connected to a force transducer (LSb200, Futek) mounted on a micromanipulator, as described in Meresman et al.[68] From the force-displacement data we estimated the flexural stiffness (EI) of the wing, assuming that it behaves as an Euler-Bernoulli beam, i.e.:

$$EI \propto \frac{FL^3}{\beta}$$

where F is the force [N] required to displace the vein junction by β [m] and L is the distance [m] from the fixed wing root to the pressed vein junction. To obtain the scaling of EI with wing length, we averaged for each wing the EI measured from the $\beta = 1$ and 2 mm displacements and then log-transformed the data to find the least-square linear relationship with log(R). Since insect wings start to dry once removed and stiffen over time,[69] we evaluated the effect of using dry wings on our scaling analysis by repeating the experiment using the same wings, after soaking them in water for 24 hours. Following removal from the water, the wings were delicately blotted with a paper towel and measured within less than 10 minutes. We noted that the soaked wings appeared to be more compliant than freshly removed beetle wings.

Revolving wing deformation test

The deformation of the revolving wings was measured using two high-speed cameras (1,000 frames s^{-1}) following the technique described by Meresman and Ribak.[33] The deflection was measured at three specific landmarks on the trailing edge (Figure 4A) by measuring the 3D positions of these landmarks using two spatially-calibrated[66] high-speed cameras (Fastcam SA3, Photron) and comparing the measured positions to their expected positions on a rigid wing, calculated based on three other landmarks on the leading edge.[33] The three trailing-edge landmarks were positioned between 0.27R and 0.65R of the wing length. We focused on this region since it is expected to bear the largest aerodynamic loads.[70,71] This technique measures instantaneous deformations in a single movie frame. We averaged the deflection from 2-6 frames from different revolution cycles and also averaged the data from the two wings in each pair.

Micro-CT scanning

We scanned five *B. rufomaculata* wing pairs $R = \{3.0, 3.5, 4, 4.5, 5.0$ cm$\}$ with a μ-CT (XT H 225 ST, Nikon Metrology NV, Leuven, Belgium), operated using a 225 kV 225 W reflection target utilizing the following scan parameters: 45 μm, 160 kV, 231 μA. The wings were glued at their hinge to a wooden pole and placed vertically in the scanning area. Despite repeated attempts, the scanning of the smallest wings provided unreliable data, likely due to the wing experiencing minute fluttering during the measurement. Consequently, we had to exclude two 3 cm long wings and one 3.5 cm long wing from the analysis. The scanned data were imported to the commercial software Dragonfly (Comet group) to measure the diameters of the veins' cross-section at seven specific locations on the wing vein structure (Figure 7). At each location, four diameter measurements were made: two diameters were parallel to connection of the wing membrane to the two sides of the vein (i.e., in the local membrane plane), comprising the external and internal diameter of the vein in this plane (dhe and dhi in Figure 6A, respectively); and two diameters were perpendicular and included the external and internal diameters out of the membrane plane (dve and dvi, respectively). Subtracting the internal diameter from the external one gave the total wall thickness (both sides) of the vein at the specific position and plane. Point 'G' in Figure 6 was an exception because the vein had a U-shaped cross-section, rather than a closed geometry. The dhi and dhe were measured as described above, while the dve and dvi were measured by drawing a line connecting the membrane from both sides of the U-shape and

measuring the distance from this line to the bottom of the U with and without the thickness of the bottom itself. While we denote the diameter measurements as in-plane and out-of plane based on the local connection of the membrane to the veins, in practice the local membrane plane had an angle θ with the global plane of the wing. θ did not change with wing size but did change between veins or even at different locations along the same vein, resulting in a rotation of the measured diameters.

PIV set-up and data analysis

The flow experiments used the same revolving wing set-up described above with $r = 2.5$ cm, $R = 4.5$ cm, and AoA = {20°, 30°, 40°}. We characterized the flow beneath the revolving wings using Particle Image Velocimetry (PIV). The wing-tip speed was 7 ms^{-1}, giving a chord-based ($\bar{c}$ = 15 mm) Reynolds number of Re_c = 7,000, corresponding to a wing-beat frequency of ~25 Hz. The 2D PIV measurement employed a dual cavity Nd:YAG laser emitting 200 mJ/pulse at 15 Hz with a 532 nm wavelength. Light-sheet forming optics illuminated a streamwise-spanwise plane downstream 2 cm below the wing. This field of view enabled us to study the downwash region formed by the rotational motion of the wing. A double-exposure 29MPixel CCD camera operating at 1 Hz with a 12-bit dynamic range was mounted vertically under the chamber glass, enabling us to image the illuminated flow field (20×20 cm^2) beneath the wings. Each experimental set involved the capture of 500 image pairs, yielding 500 instantaneous vector maps, from which the averaged velocities were determined, allowing for statistical convergence per AoA. The PIV analysis used a 64×64 interrogation window with an overlap of 50%. Standard Gaussian and median filters were applied to the data to remove erroneous vectors filled by cubic interpolated data.

QUANTIFICATION AND STATISTICAL ANALYSIS

When relevant, sample sizes are described in the figure legends. Mean values are reported ± 1 standard error unless specifically specified otherwise.